available for this purpose. In this paper, we took advantage of the thermal sensitivity of tyrosinase to explore the possibility that tyrosinase folding can be manipulated. We initially examined various naturally occurring temperature-sensitive tyrosinase mutants such as R402Q, P406L, and R422Q (30). However, their thermally induced misfolding was not very reversible and therefore not suitable for experiments to study maturation.[2] However, the folding of wild type tyrosinase was dependent on the incubation temperature, as we were able to show using DOPA oxidase activity as a folding marker (Fig. 1A). Although incubation at the permissive temperature did not resolve the structure to the completely native structure (Fig. 4A), the molecule still acquired COPII-dependant exportability from the ER (Figs. 4C and 6A) as well as full DOPA oxidase activity (Fig. 1A). We reasoned that these properties were adequate to study the dynamic properties of a maturing cargo protein in the ER.

At present, the expression of chimeric proteins tagged with a fluorescent protein is the only way to study diffusion in living cells. We noticed that the conventional methods for transiently expressing tyrosinase-YFP using lipophilic compounds generally resulted in massive photobleaching when measured with a FCS setup. As a result, we first determined how expression levels affect photobleaching using a glass bead-loading method (42) (Fig. 1C). The relationship suggests that any detectable levels of folded tyrosinase-YFP expression significantly influence diffusion in the ER, but as long as the expression level is below a threshold, random diffusion should be measurable. We estimated that tyrosinase-YFP would not be "saturated" in our setup if the expression level was less than 100 kHz. If we assume that the diameter of folded tyrosinase is smaller than 10 nm and if the fluorescence count per single molecule is higher than 3 kHz, as observed, this estimation seems reasonable because the confocal volume (~0.2 fl), which is estimated to contain fewer than 33 molecules, is far larger than the volume that tyrosinase-YFP occupies. Our first conclusion was that the observed diffusion was markedly suppressed at the non-permissive temperature, as measured with FCS. This is based on the results that thermally misfolded tyrosinase showed extensive photobleaching irrespective of the expression level (Fig. 2A). As a result of the limited fluctuation, the autocorrelation function could not be applied to this measurement (Fig. 2B, *top panel*, and C). It is conceivable that this result was caused by the formation of extremely large aggregates. However, this is unlikely because the apparent molecular size of the thermally misfolded tyrosinase was no larger than that synthesized in the presence of castanospermine (Fig. 4A).

We thus conjectured that these data indicate a status where random diffusion is restricted by the cellular machinery. This regulation would presumably help to prevent irreversible misfolding because of large aggregate formation by reducing the chance of collision between proteins with exposed hydrophobic patches on their surfaces, and would thereby function to maintain foldability in stressful conditions. Various responses to stress include suppression of translation, induction of heat-shock proteins, and enhanced degradation of misfolded proteins (48). In general, it is thought that aggregation is prevented by the repeated binding of molecular chaperones. Our conclusion may indicate that there is another cellular mechanism that is used to avoid the formation of aggregates, which are thought to be toxic (49–51). Indeed, thermally misfolded tyrosinase showed no particular cytotoxicity, in that it was possible to obtain COS7 cells stably expressing misfolded tyrosinase by culturing them at 40 °C.[2] This may be partly because of the proposed restriction of random diffusion to prevent the formation of aggregates. The observed slow diffusion could be

caused by either a regulated association with the immobile matrix or the association with a matrix whose diffusion is thermally regulated. One candidate for the matrix is the ER chaperone network, which is composed of weakly interacting molecular chaperones and folding enzymes (15, 16). Alternatively, it is possible that cells contain protective structures whose phase or conformation is altered upon heat shock.

Similar restriction of diffusion has been described in several reports. For example, in an analysis of protein transport in the plastid tubules of the tobacco plant, two-photon FCS revealed that spontaneous diffusion of expressed green fluorescent proteins in plastids was ~50 times slower than that in the cytosol (52). Interestingly, they found that the FCS recordings included the presence of ATP-dependent active transport, which alternated with "dim periods" in which only random diffusion was seen. This active transport could function to provide long-range transport in a 50-μm plastid tubule. They suggested that the low diffusion coefficient may be caused by fluid-phase viscosity. Similarly, mitochondrial matrix proteins are thought to have slow diffusion because of steric hindrance because of a very high protein concentration in the compartments (53). Interestingly, the dynamics of proteins in the matrix is rather anomalous. Partikian *et al.* (54) showed that green fluorescent protein expressed in the matrix was as highly mobile as in water, although large enzyme complexes in the matrix were almost immobilized, suggesting that the mitochondrial matrix is organized into a highly viscous peripheral area and a central region with low protein density. Another well known example is the nuclear proteins. Extensive FRAP analysis has revealed that molecules in the nucleus show highly diverse dynamics (reviewed by Refs. 55–59) that most likely depend on their associations with DNA, which is nearly immobile on a time scale of several minutes (60).

We thus think that the regulation of immature tyrosinase mobility occurs on at least two different levels. At present, our preferred model is that the FRAP-detectable diffusion may be a result of the cellular machinery for facilitated diffusion in the ER network. Considering that immature proteins are transported through the narrow hollow tubules of the ER to the punctate COPII-coated sites, and that the diameter of the ER tubules are only a few times larger than those of average mature proteins, it is not surprising that active transport of molecules in the ER is required for efficient maturation. Indeed, our current research indicates that the mobility of certain proteins in the ER is regulated.[3] Further studies on the dynamics of maturing proteins should help to understand why folding is so successful in healthy cells continuously exposed to various types of folding stresses that easily terminate folding *in vitro*.

REFERENCES

1. Matlack, K. E., Misselwitz, B., Plath, K., and Rapoport, T. A. (1999) *Cell* **97**, 553–564
2. Kornfeld, R., and Kornfeld, S. (1985) *Annu. Rev. Biochem.* **54**, 631–664
3. Stevens, F. J., and Argon, Y. (1999) *Semin. Cell Dev. Biol.* **10**, 443–454
4. Ferrari, D. M., and Soling, H. D. (1999) *Biochem. J.* **339**, 1–10
5. Freedman, R. B., Klappa, P., and Ruddock, L. W. (2002) *EMBO Rep.* **3**, 136–140
6. Bose, S., and Freedman, R. B. (1994) *Biochem. J.* **300**, 865–870
7. Fewell, S. W., Travers, K. J., Weissman, J. S., and Brodsky, J. L. (2001) *Annu. Rev. Genet.* **35**, 149–191
8. Benham, A. M., and Braakman, I. (2000) *Crit. Rev. Biochem. Mol. Biol.* **35**, 433–473
9. Lord, J. M., Ceriotti, A., and Roberts, L. M. (2002) *Curr. Biol.* **12**, R182–R184
10. Jarosch, E., Geiss-Friedlander, R., Meusser, B., Walter, J., and Sommer, T. (2002) *Traffic* **3**, 530–536
11. Braakman, I. (2001) *EMBO Rep.* **2**, 666–668
12. Gallione, C. J., and Rose, J. K. (1985) *J. Virol.* **54**, 374–382
13. Doms, R. W., Keller, D. S., Helenius, A., and Balch, W. E. (1987) *J. Cell Biol.*

105, 1957–1969
14. Hammond, C., and Helenius, A. (1994) *J. Cell Biol.* **126**, 41–52
15. Tatu, U., and Helenius, A. (1997) *J. Cell Biol.* **136**, 555–565
16. Meunier, L., Usherwood, Y. K., Chung, K. T., and Hendershot, L. M. (2002) *Mol. Biol. Cell* **13**, 4456–4469
17. Axelrod, D., Koppel, D. E., Schlessinger, J., Elson, E., and Webb, W. W. (1976) *Biophys. J.* **16**, 1055–1069
18. Nehls, S., Snapp, E. L., Cole, N. B., Zaal, K. J., Kenworthy, A. K., Roberts, T. H., Ellenberg, J., Presley, J. F., Siggia, E., and Lippincott-Schwartz, J. (2000) *Nat. Cell Biol.* **2**, 288–295
19. Hendershot, L. M. (2000) *Nat. Cell Biol.* **2**, E105–E106
20. Rigler, R., and Elson, E. L. (2001) *Fluorescence Correlation Spectroscopy: Theory and Applications*, Springer-Verlag, Berlin
21. Elson, E. L. (2001) *Traffic* **2**, 789–796
22. Hess, S. T., Huang, S., Heikal, A. A., and Webb, W. W. (2002) *Biochemistry* **41**, 697–705
23. Widengren, J., and Rigler, R. (1998) *Cell. Mol. Biol. (Noisy-le-grand)* **44**, 857–879
24. Foldes-Papp, Z., Demel, U., and Tilz, G. P. (2001) *Proc. Natl. Acad. Sci. U. S. A.* **98**, 11509–11514
25. Larson, D. R., Ma, Y. M., Vogt, V. M., and Webb, W. W. (2003) *J. Cell Biol.* **162**, 1233–1244
26. Terada, S., Kinjo, M., and Hirokawa, N. (2000) *Cell* **103**, 141–155
27. Hearing, V. J. (1987) *Methods Enzymol.* **142**, 154–165
28. Spritz, R. A., and Hearing, V. J. (1994) in *Advances in Human Genetics* (Hirschhorn, K., and Harris, H., eds) pp. 1–5, Plenum Press, New York
29. Halaban, R., Svedine, S., Cheng, E., Smicun, Y., Aron, R., and Hebert, D. N. (2000) *Proc. Natl. Acad. Sci. U. S. A.* **97**, 5889–5894
30. Toyofuku, K., Wada, I., Spritz, R. A., and Hearing, V. J. (2001) *Biochem. J.* **355**, 259–269
31. Berson, J. F., Frank, D. W., Calvo, P. A., Bieler, B. M., and Marks, M. S. (2000) *J. Biol. Chem.* **275**, 12281–12289
32. Petrescu, S. M., Petrescu, A. J., Titu, H. N., Dwek, R. A., and Platt, F. M. (1997) *J. Biol. Chem.* **272**, 15796–15803
33. Halaban, R., Cheng, E., Zhang, Y., Moellmann, G., Hanlon, D., Michalak, M., Setaluri, V., and Hebert, D. N. (1997) *Proc. Natl. Acad. Sci. U. S. A.* **94**, 6210–6215
34. Branza-Nichita, N., Petrescu, A. J., Dwek, R. A., Wormald, M. R., Platt, F. M., and Petrescu, S. M. (1999) *Biochem. Biophys. Res. Commun.* **261**, 720–725
35. Toyofuku, K., Wada, I., Hirosaki, K., Park, J. S., Hori, Y., and Jimbow, K. (1999) *J. Biochem. (Tokyo)* **125**, 82–89
36. Honing, S., Sandoval, I. V., and von Figura, K. (1998) *EMBO J.* **17**, 1304–1314

37. Simmen, T., Schmidt, A., Hunziker, W., and Beermann, F. (1999) *J. Cell Sci.* **112**, 45–53
38. Calvo, P. A., Frank, D. W., Bieler, B. M., Berson, J. F., and Marks, M. S. (1999) *J. Biol. Chem.* **274**, 12780–12789
39. Setaluri, V. (2000) *Pigment Cell Res.* **13**, 128–134
40. Jimbow, K., Park, J. S., Kato, F., Hirosaki, K., Toyofuku, K., Hua, C., and Yamashita, T. (2000) *Pigment Cell Res.* **13**, 222–229
41. Hirosaki, K., Yamashita, T., Wada, I., Jin, H. Y., and Jimbow, K. (2002) *J. Investig. Dermatol.* **119**, 475–480
42. Nagaya, H., Wada, I., Jia, Y.-J., and Kanoh, H. (2002) *Mol. Biol. Cell* **13**, 302–316
43. Akagi, T., Shishido, T., Murata, K., and Hanafusa, H. (2000) *Proc. Natl. Acad. Sci. U. S. A.* **97**, 7290–7295
44. Spector, D. L., Goldman, R. D., and Leinwand, L. A. (1997) *Cells: A Laboratory Manual*, Vol. 2, Cold Spring Harbor Laboratory Press, Cold Spring Harbor, NY
45. Misumi, Y., Miki, K., Takatsuki, A., Tamura, G., and Ikehara, Y. (1986) *J. Biol. Chem.* **261**, 11398–11403
46. Swaminathan, R., Hoang, C. P., and Verkman, A. S. (1997) *Biophys. J.* **72**, 1900–1907
47. Rose, J. K., and Gallione, C. J. (1981) *J. Virol.* **39**, 519–528
48. Mori, K. (2003) *Traffic* **4**, 519–528
49. Bence, N. F., Sampat, R. M., and Kopito, R. R. (2001) *Science* **292**, 1552–1555
50. Bucciantini, M., Giannoni, E., Chiti, F., Baroni, F., Formigli, L., Zurdo, J., Taddei, N., Ramponi, G., Dobson, C. M., and Stefani, M. (2002) *Nature* **416**, 507–511
51. Dobson, C. M. (2003) *Nature* **426**, 884–890
52. Kohler, R. H., Schwille, P., Webb, W. W., and Hanson, M. R. (2000) *J. Cell Sci.* **113**, 3921–3930
53. Welch, G. R., and Easterby, J. S. (1994) *Trends Biochem. Sci.* **19**, 193–197
54. Partikian, A., Olveczky, B., Swaminathan, R., Li, Y., and Verkman, A. S. (1998) *J. Cell Biol.* **140**, 821–829
55. Misteli, T. (2001) *Science* **291**, 843–847
56. Misteli, T. (2001) *J. Cell Biol.* **155**, 181–185
57. Phair, R. D., and Misteli, T. (2001) *Nat. Rev. Mol. Cell. Biol.* **2**, 898–907
58. Festenstein, R., Pagakis, S. N., Hiragami, K., Lyon, D., Verreault, A., Sekkali, B., and Kioussis, D. (2003) *Science* **299**, 719–721
59. Cheutin, T., McNairn, A. J., Jenuwein, T., Gilbert, D. M., Singh, P. B., and Misteli, T. (2003) *Science* **299**, 721–725
60. Lukacs, G. L., Haggie, P., Seksek, O., Lechardeur, D., Freedman, N., and Verkman, A. S. (2000) *J. Biol. Chem.* **275**, 1625–1629

Direct detection of caspase-3 activation in single live cells by cross-correlation analysis☆

Kenta Saito[a], Ikuo Wada[b], Mamoru Tamura[a], Masataka Kinjo[a],*

[a] *Laboratory of Supramolecular Biophysics, Research Institute for Electronic Science, Hokkaido University, N12W6, Kita-ku, Sapporo 060-0812, Japan*
[b] *Department of Cell Science, Institute of Biomedical Sciences, Fukushima Medical University, 1-Banchi, Hikarigaoka, Fukushima 960-1295, Japan*

Abstract

Dual color fluorescence cross-correlation spectroscopy (FCCS) provides information about the coincidence of spectrally well-defined two fluorescent molecules in a small observation area at the single-molecule level. To evaluate the activity of caspase-3 in vivo directly, FCCS was applied to single live cells. We constructed chimeric proteins that consisted of tandemly fused enhanced green FP (EGFP) and monomeric red FP (mRFP). In control experiments, the protease reaction was monitored in solution, where a decrease in cross-correlation amplitude was observed due to specific cleavage of the amino acid sequence between EGFP and mRFP. Moreover, a decrease in cross-correlation amplitude could be detected in a live cell, where caspase-3 activation was induced by apoptosis. This is the first report of FP-based in vivo cross-correlation analysis. FP-based FCCS may become the most versatile method for analysis of protein–protein interactions in live cells.
© 2004 Elsevier Inc. All rights reserved.

The fluorescence resonance energy transfer (FRET) technique has been used for studying protein–protein interactions in live cells [1]. However, because FRET efficiency strongly depends on the distance between donor and acceptor fluorophores (~10 nm) even in their appropriate angle, the sizes of the target molecule, and/or interaction molecule are greatly limited.

Instead, fluorescence correlation spectroscopy (FCS) [2] can be applied for this purpose, as it provides information about the mobility of fluorescently tagged target molecules at a very low concentration (~pM) in vitro [3,4] and in vivo [5–8]. FCS measurement is based on single photon counting at the single-molecule level in a defined detection volume (~0.25 fl) generated by an excitation laser beam and fine detection optics. The diffusion constant and the concentration of target molecules can be determined from the auto-correlation function ($G(\tau)$), allowing us to monitor their interactions in situ [3,4,8].

An extended technique of FCS, dual color fluorescence cross-correlation spectroscopy (FCCS), can detect the coincidence of two spectrally distinct fluorescent probes in a small detection area at very low concentrations [9–11]. In principle, this technique is free from the limitations of FRET. FCCS has been used to detect the association–dissociation reaction and interaction between two molecular species in vitro [12–15]. Only a very few attempts have so far been made at the cross-correlation analysis of live cells [16,17]. Herein, we will report the usefulness of fluorescent protein (FP)-based cross-correlation analysis of live cells. For the quantitative

evaluation of cross-correlation, we constructed a chimeric protein in which enhanced green FP (EGFP) is fused to monomeric red FP (mRFP) [18] via two types of 29 linker sequences cleaved by either enterokinase [19] or caspase-3 [20]. For the first time, we report here that caspase-3 reaction can be detected in vitro and in vivo through the decrease of cross-correlation amplitude due to protease cleavage of a specific recognition sequence between EGFP and mRFP.

Experimental procedures

Cell preparation. HeLa cells were grown in a 5% CO_2 humidified atmosphere at 37 °C in Dulbecco's modified Eagle's medium (DMEM) supplemented with 10% fetal bovine serum, 2×10^5 U/L penicillin G, and 200 mg/L streptomycin sulfate. Transfection of HeLa cells grown on LAB-TEK chambered coverslips with eight wells (Nalge Nunc International) was performed using FuGENE 6 (Roche Molecular Biochemicals). During FCCS measurements, HeLa cells were maintained in Opti-MEM I reduced-serum medium (Invitrogen).

Plasmid construction. Enterokinase (ek) or caspase-3 (c3) recognition sites were engineered in the N-terminus of mRFP (R) or tandem mRFP dimer (R_2) by polymerase chain reaction (PCR). The PCR products were digested and ligated into the multiple cloning site of pEGFP-C1 (Clontech). These plasmids encode EGFP (G) and R or R_2 fusion proteins (EGFP-mRFP chimera), G-X-R and G-X-R_2, in which X = D_4K in the case of enterokinase recognition site, X = DEVD in the case of caspase-3 recognition site.

Protease assay. Proteins (G, R, R_2, G-X-R, and G-X-R_2) for in vitro measurements were produced using a wheat germ extract (cell-free) translation system [21]. First, 10.0 µl of EGFP-mRFP chimera was incubated with 0.016 U/µl of recombinant enterokinase (Novagen) at room temperature. The enterokinase reaction mixture contained 20 mM Tris-HCl, pH 7.4, 50 mM NaCl, and 2 mM $CaCl_2$. Then 10.0 µl of EGFP-mRFP chimera was incubated with 1.0 U/µl caspase-3 (Calbiochem) at 37 °C. The caspase-3 reaction mixture contained 20 mM Hepes-KOH, pH 7.4, 10 mM KCl, 1.5 mM $MgCl_2$, 1 mM EDTA, 1 mM EGTA, and 10 mM DTT. For in vivo protease reaction assay, HeLa cells were treated with 50 ng/ml tumor necrosis factor-α (TNF-α) and 10 µg/ml cycloheximide (CHX).

Microscopy. Live cell fluorescence imaging was performed using an inverted confocal laser scanning microscope LSM510 (Carl Zeiss). EGFP was excited at the 488 nm laser line of a CW Ar^+ laser and mRFP was excited at the 543 nm laser line of a CW He–Ne laser through a water immersion objective (C-Apochromat, 40×, 1.2NA; Carl Zeiss). Emission signals were detected at 505–550 nm for EGFP and >560 nm for mRFP by sequential scanning.

FCCS measurement. FCCS measurements were carried out mainly with a ConfoCor2 (Carl Zeiss), which consisted of a CW Ar^+ laser and He–Ne laser, a water immersion objective (C-Apochromat, 40×, 1.2NA; Carl Zeiss), and two channels of avalanche photodiodes (SPCM-200-PQ; EG&G). The confocal pinhole diameter was adjusted to 90 µm. EGFP was excited at the 488 nm laser line and mRFP was excited at the 543 nm laser line. The emission signals were split by a dichroic mirror (570 nm beam splitter) and detected at 505–530 nm by the green channel for EGFP and at 600–650 nm by the red channel for mRFP. FCCS measurements were also carried out with a Leica FCS system (Leica). In this system, EGFP was excited at the 488 nm laser line and mRFP was excited at the 594 nm laser line. Emission signals were detected at 505–530 nm for EGFP and 607–683 nm for mRFP.

Data analysis. The fluorescence auto-correlation functions of the red and green channels, $G_r(\tau)$ and $G_g(\tau)$, and the fluorescence cross-correlation function, $G_c(\tau)$, are calculated by

$$G_x(\tau) = \frac{\langle \delta I_i(t) \cdot \delta I_j(t+\tau) \rangle}{\langle I_i(t) \rangle \langle I_j(t) \rangle}, \tag{1}$$

where τ denotes the time delay, I_i is the fluorescence intensity of the red channel ($i = r$) or green channel ($i = g$), $G_r(\tau)$, $G_g(\tau)$, and $G_c(\tau)$ denote the auto-correlation functions of red ($i = j = x = r$), green ($i = j = x = g$), and cross ($i = r$, $j = g$, and $x = c$), respectively. Acquired $G(\tau)$ were fitted by a one-, two-, or three-component model as

$$G(\tau) = \frac{1}{N}\sum_i F_i \left(1 + \frac{\tau}{\tau_i}\right)^{-1} \left(1 + \frac{\tau}{s^2\tau_i}\right)^{-1/2}, \tag{2}$$

where F_i and τ_i are the fraction and diffusion time of component i, respectively. N is the average number of fluorescent particles in the excitation-detection volume defined by radius w_0 and length $2z_0$, and s is the structure parameter representing the ratio $s = z_0/w_0$. The average numbers of red fluorescent particles (N_r), green fluorescent particles (N_g), and particles that have both red and green fluorescence (N_c) can be calculated by

$$N_r = \frac{1}{G_r(0)}, \quad N_g = \frac{1}{G_g(0)}, \quad \text{and } N_c = \frac{G_c(0)}{G_r(0) \cdot G_g(0)}, \tag{3}$$

respectively. When N_r and N_g are constant, $G_c(0)$ is directly proportional to N_c. For quantitative evaluation of cross-correlation among various samples, $G_c(0)$ is normalized by $G_g(0)$ (relative cross-correlation amplitude; $G_c(0)/G_g(0)$).

Results

In vitro control experiments

To assess the degree of cross-correlation ($G_c(\tau)$); see experimental procedures quantitatively, FCCS measurements were carried out with purified proteins in PBS. Since the brightness of mRFP is very weak [18], to improve it, we also constructed another probe in which additional mRFP coding sequence was inserted after an EGFP-mRFP chimera (EGFP fused to tandem mRFP dimer). Fluorescent intensity at the red channel of the G-DEVD-R_2 was about 2-fold that of G-DEVD-R (Figs. 1A and C, insets). A mixture of EGFP and mRFP, which are referred to as MixGR and MixGR$_2$, were used as control samples against the linked proteins, G-DEVD-R and G-DEVD-R_2. The concentrations of the mixture of EGFP and mRFP, MixGR, and MixGR$_2$ were prepared to have the roughly the same green and red fluorescent intensity ratios as the EGFP-mRFP chimera (Figs. 1A–D, insets). Amplitudes of auto-correlation curves were almost the same for G-DEVD-R and MixGR (Figs. 1A and B), and for G-DEVD-R_2 and MixGR$_2$ (Figs. 1C and D). In contrast, amplitudes of cross-correlation were only apparent in G-DEVD-R and G-DEVD-R_2 (Figs. 1A and C) but almost absent in a mixture of EGFP and mRFP (Figs. 1B and D). We considered that the small value $G_c(0)/G_g(0)$ of the mixture of EGFP and mRFP (Table 1) was the background due to the leakage of EGFP emission through the red channel detector (red detector cross-talk) because $G_c(0)/G_g(0)$ of mixture of EGFP and mRFP became larger at a higher EGFP
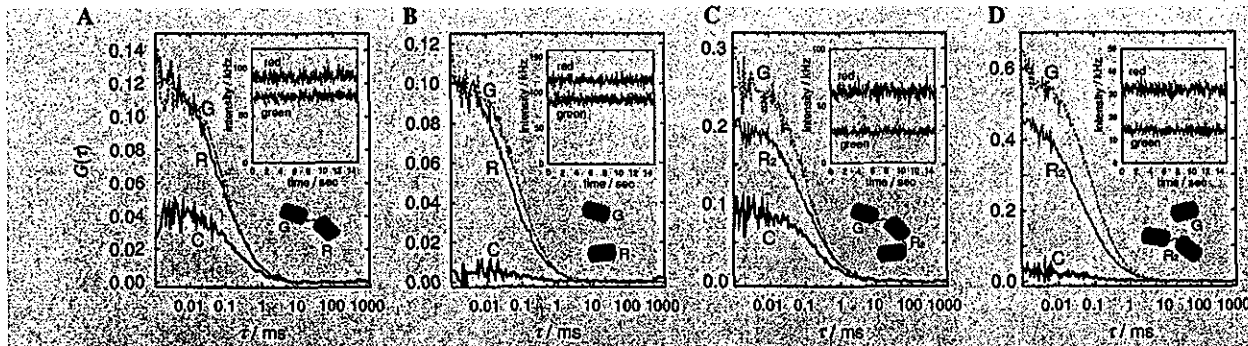
Fig. 1. In vitro cross-correlation analysis. Typical auto- and cross-correlation curves of (A) G-DEVD-R, (B) MixGR, (C) G-DEVD-R₂, and (D) MixGR₂ in PBS. (Insets) The fluorescence intensities in red and green channels during FCCS measurement. R, G, and C represent $G_r(\tau)$, $G_g(\tau)$, and $G_c(\tau)$, respectively. (For interpretation of the references to colours in this figure legend, the reader is referred to the web version of this paper.)

Table 1
Relative cross-correlation amplitude $G_c(0)/G_g(0)$

EGFP-mRFP chimera		Mixture of EGFP and mRFP	
Sample	$G_c(0)/G_g(0)$	Sample	$G_c(0)/G_g(0)$
In PBS			
G-DEVD-R	0.369 ± 0.006	MixGR	0.088 ± 0.002
G-DEVD-R₂	0.373 ± 0.007	MixGR₂	0.035 ± 0.006
In HeLa cells			
G-DEVD-R	0.467 ± 0.028	MixGR	0.233 ± 0.020
G-DEVD-R₂	0.391 ± 0.037	MixGR₂	0.102 ± 0.008
G-D₄K-R₂	0.394 ± 0.032	—	—
In apoptotic HeLa cells			
G-DEVD-R₂	0.047 ± 0.005	—	—
G-D₄K-R₂	0.237 ± 0.031	—	—

Values are means ± SD for three in vitro measurements and for six in vivo measurements.

concentration and smaller at a higher mRFP concentration (data not shown). We found that G-DEVD-R₂ is a sensitive probe compared to G-DEVD-R because the ratio of relative amplitude between G-DEVD-R₂ and MixGR₂ was higher than that of G-DEVD-R and MixGR (Table 1). By using auto-correlation analysis, it is impossible to distinguish G-DEVD-R₂ from MixGR₂ since the diffusion time of G-DEVD-R2 was only two times larger than that of MixGR2 (data not shown). We thus concluded that cross-correlation could clearly discriminate the difference of coincidence of linked FPs and unlinked FPs.

Real-time monitoring of protease reaction in vitro

In the EGFP-mRFP chimera, addition of protease should reduce cross-correlation amplitude $G_c(0)$. The protease reaction results in release of EGFP and mRFPs that may cause reduction of cross-correlation amplitude $G_c(0)$. Because N_r and N_g are constant during the protease reaction, $G_c(0)$ is directly proportional to the number of linked proteins N_c. The decrease of the intact

G-D₄K-R₂ concentration could be monitored as a reduction of $G_c(0)/G_g(0)$. We thus measured how cross-correlation amplitude of G-D₄K-R₂ was altered upon addition of enterokinase (Fig. 2A). $G_c(0)$ of G-D₄K-R₂ was gradually reduced after adding 0.016 U/μl enterokinase. Fluorescence intensities in red and green channels were constant during the protease reaction (Fig. 2A, inset) and auto-correlation amplitudes $G_r(0)$ and $G_g(0)$ were also largely unchanged (data not shown). This suggested that no FRET occurred between EGFP and mRFP in intact G-D₄K-R₂ and also that the protease cleaved only the specific recognition sequence. $G_c(0)/G_g(0)$ of G-D₄K-R₂ was reduced to 20% and reached a plateau at 400 s after 0.016 U/μl enterokinase addition. We found that the reaction rate was proportional to the amount of the enzyme used (Fig. 2B). In contrast, no change of $G_c(0)/G_g(0)$ without enterokinase was observed. Then, the same time course as for FCCS measurements was used for real time monitoring of the cleavage process of 30 nM G-DEVD-R₂ after caspase-3 addition. $G_c(0)$ of G-DEVD-R₂ was slowly reduced after adding 1.0 U/μl caspase-3 at 37 °C (Fig. 2C). $G_c(0)/G_g(0)$ of G-DEVD-R₂ was reduced after adding caspase-3 (Fig. 2D) though the decay of $G_c(0)/G_g(0)$ of G-D₄K-R₂ was slower than that of G-DEVD-R2 at the same caspase-3 concentration. This demonstrated that the protease cleavage process could be simply monitored in real time by cross-correlation analysis as an 80% decrease of $G_c(0)$ in the small substrate concentration at a variable enzyme concentration (Fig. 2A) with specific recognition sequence (Fig. 2C).

In vivo control experiments

Next, we applied this strategy to the EGFP-mRFP chimera expressed in HeLa cells. At the beginning of measurements, strong photobleaching of mRFP occurred even at the same excitation laser power as in vitro. Consequently, the fluorescent intensity of the red channel decreased to about 1/3 and $G_r(0)$ increased about 3-fold
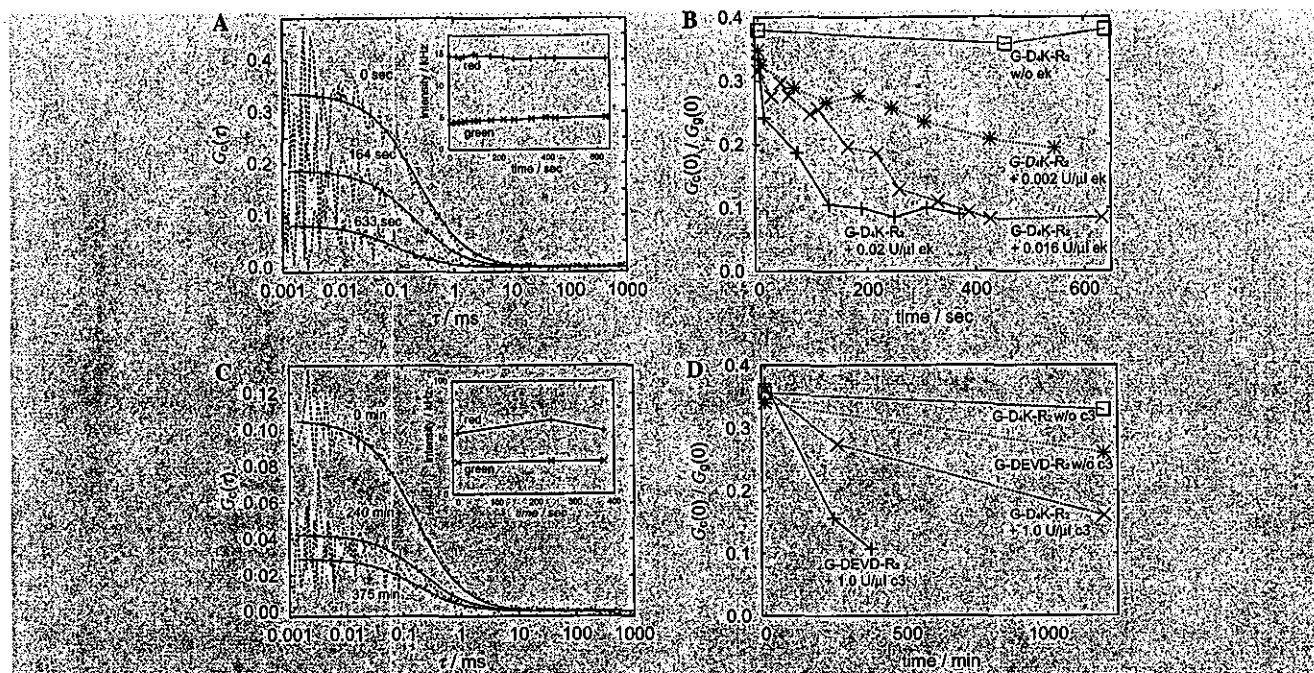
Fig. 2. Kinetics of protease reaction in vitro. (A) $G_c(\tau)$ of G-D$_4$K-R$_2$ in the time after 0.016 U/µl enterokinase addition. The dotted lines show measured curves and the solid lines show their fitted curves. (Inset) Time courses of the fluorescence intensities in red and green channels. (B) Relative cross-correlation amplitude, $G_c(0)/G_g(0)$ after the addition of various concentrations of enterokinase (eK). The concentration of G-D$_4$K-R$_2$ estimated from the amplitude of $G_g(\tau)$ was about 10 nM. (C) $G_c(\tau)$ of G-DEVD-R$_2$ in the time after 1.0 U/µl caspase-3 addition. The solid lines are measured curves and the dotted lines are their fitted curves. (Inset) Time courses of fluorescence intensities of red and green channels. (D) Relative cross-correlation amplitude, $G_c(0)/G_g(0)$ after the addition of caspase-3 (c3). Concentration of G-D$_4$K-R$_2$ estimated from the amplitude of $G_g(\tau)$ was about 30 nM. (For interpretation of the references to colours in this figure legend, the reader is referred to the web version of this paper.)
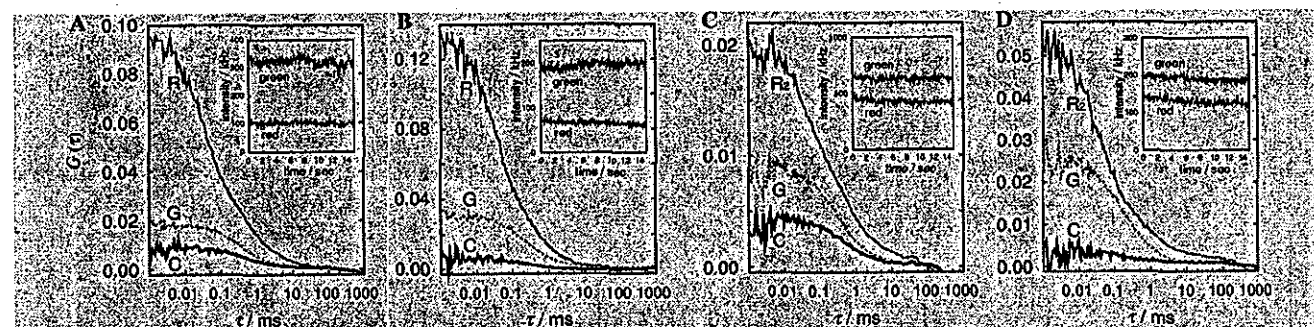
Fig. 3. Live cell cross-correlation analysis. Typical auto- and cross-correlation curves of (A) G-DEVD-R, (B) MixGR, (C) G-DEVD-R$_2$, and (D) MixGR$_2$ expressed in HeLa cells. (Insets) The fluorescence intensities in red and green channels during FCCS measurement. R, G, and C represent $G_r(\tau)$, $G_g(\tau)$, and $G_c(\tau)$, respectively.

(Fig. 3). In addition, $G_c(0)/G_g(0)$ of mixture of EGFP and mRFP, which indicates the background due to the red detector cross-talk, was larger than that of in vitro measurements (Table 1). These results were indicative of difficulties of in vivo measurements, however, we were able to obtain significant cross-correlation signal in a EGFP fused to a tandem mRFP dimer.

Detection of apoptosis-induced caspase-3 activation

To assess the potentials of this technique for biological application, we investigated FCCS-based detection of apoptosis-induced caspase-3 activation in vivo. For apoptosis induction, tumor necrosis factor-α (TNF-α), and cycloheximide (CHX) were loaded into HeLa cells. EGFP-mRFP chimera was distributed mostly in cytosol and also in the nucleus (Figs. 4A and C, insets). We selected cells which were weakly fluorescent to obtain sufficient amplitudes of auto-and cross-correlation. Cross-correlation signals of G-DEVD-R$_2$ and G-D$_4$K-R$_2$ in intact HeLa cells were same (Figs. 4A and C). Apoptotic morphological changes were observed at 3 h after TNF-α and CHX treatment (Figs. 4B and D, insets). In apoptotic HeLa cells, the cross-correlation
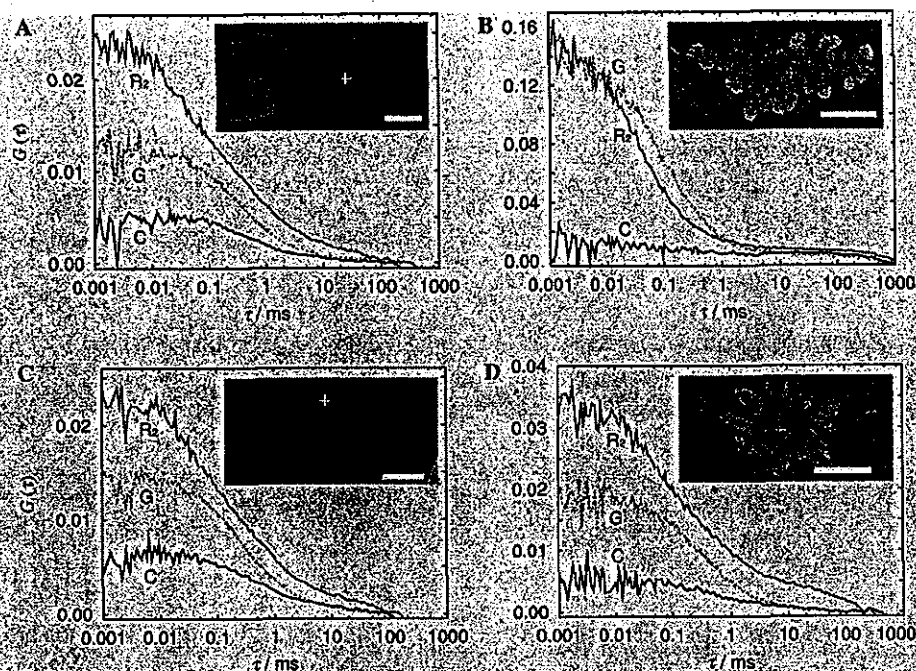
Fig. 4. Detection of caspase-3 activation in apoptotic HeLa cells. Typical auto- and cross-correlation spectroscopy of G-DEVD-R₂ (A) before and (B) after apoptosis induction and those of G-D₄K-R₂ (C) before and (D) after apoptosis induction in HeLa cells. (Insets) Measurement positions are indicated by the cross-hair (+) in the green channel laser scanning microscopy (LSM) images of G-DEVD-R₂ and G-D₄K-R₂ transiently expressed in HeLa cells. R, G, and C represent $G_r(\tau)$, $G_g(\tau)$, and $G_c(\tau)$, respectively. Scale bar represents 10 μm. (For interpretation of the references to colours in this figure legend, the reader is referred to the web version of this paper.)

amplitude of G-DEVD-R₂ was reduced (Fig. 4B). $G_c(0)/G_g(0)$ of G-DEVD-R₂ in apoptotic HeLa cells was as low as in the control, $G_c(0)/G_g(0)$ of MixGR₂ in intact HeLa cells (Table 1). On the other hand, even in apoptotic HeLa cells, the cross-correlation amplitude of G-D₄K-R₂ was maintained at a higher level because enterokinase was not distributed in the cell. While $G_c(0)/G_g(0)$ of G-D₄K-R₂ in apoptotic cells was slightly reduced, it was significantly higher than that of MixGR₂ in intact HeLa cells (Fig. 4D and Table 1). $G_c(0)/G_g(0)$ of G-D₄K-R₂ in apoptotic cells was somewhat reduced (Figs. 4C and D). It was also reduced by caspase-3 treatment in vitro (Fig. 2D). We thought the enterokinase site in the linker sequence (D₄K) is slightly susceptible to caspase-3. In apoptotic cells, there might be caspase-3, and also other protease activities induced by TNF-α. Finally, the DEVD sequence of G-DEVD-R₂ was selectively recognized by caspase-3 in live cells. These results indicate that cross-correlation analysis can detect the protease activation in vivo by the use of tandem mRFP dimer.

Discussion

By using the well-characterized proteolytic reaction of caspase-3, we have successfully showed that cross-correlation could clearly discriminate the difference of coincidence of linked FPs and unlinked FPs. We made the

linker with the length in no FRET between EGFP and mRFP occurs because analysis of FCCS would be simplified. We did not try linker sequences with different lengths however we made enough length for the linker that did not inhibit the protease activity in this experiment. One of the advantages in the FCCS method is that FCCS is applicable to the sample with various (long or short) linker sequences. It was practically insensitive to detect the cleavage of FPs upon caspase-3 reaction by auto-correlation analysis. Assuming only one-direction cross-talk (green emission into red channel), in the case of EGFP-mRFP chimera, $G_c(0)$ is expected to be constant at single mRFP and double mRFPs from expanded equation of $G(0)$ [10]. On the other hand, in the case of mixture of EGFP and mRFP, $G_c(0)$ of double mRFPs is expected to be lower than single mRFP. Our results measured in PBS were consistent with these expectations (Table 1). The quantitative analysis as described here largely depends on the construction of stoichiometrically uniform probes in which different colored probe is fused to each other at a 1:1 ratio by conventional recombinant DNA technique [22]. Previously, it was reported that chemically synthesized probes, which were heterogeneously labeled, were not ideal for sensitivity of cross-correlation analysis [16]. However, since mRFP has relatively lower brightness and susceptibility to photobleaching [18], red-shifted improvement of this probe will be beneficial. When brighter, more red-shifted and photostable mRFP becomes available, FCCS will be one of the

most sensitive tools for in vivo biochemistry. Furthermore, FCCS can also be used to study the molecular interactions over long distances such as colocalization of cargoes in the same endocytic vesicles [16] and for the detection of a large DNA sample of 4 kbp 5′-Cy5 and 5′-rhodamine green-labeled PCR products [15]. FP-based FCCS may become the most versatile method for analysis of protein–protein interactions in live cells. We believe that this fluorescent protein-based FCCS will be a reliable fluorescence analysis for other intracellular protein dynamics and must become a powerful and convenient method for the analysis of protein–protein interactions in intact cells.

References

[1] A. Miyawaki, Visualization of the spatial and temporal dynamics of intracellular signaling, Dev. Cell 4 (2003) 295–305.

[2] R. Rigler, Ü. Mets, J. Widengren, P. Kask, Fluorescence correlation spectroscopy with high count rate and low background: analysis of translational diffusion, Eur. Biophys. J. 22 (1993) 169–175.

[3] Y. Takakuwa, C.-G. Pack, X.-L. An, S. Manno, E. Ito, M. Kinjo, Fluorescence correlation spectroscopy analysis of the hydrophobic interactions of protein 4.1 with phosphatidyl serine liposomes, Biophys. Chem. 82 (1999) 149–155.

[4] C.-G. Pack, K. Aoki, H. Taguchi, M. Yoshida, M. Kinjo, M. Tamura, Effect of electrostatic interactions on the binding of charged substrate to GroEL studied by highly sensitive fluorescence correlation spectroscopy, Biochem. Biophys. Res. Commun. 267 (2000) 300–304.

[5] P. Schwille, U. Haupts, S. Maiti, W.W. Webb, Molecular dynamics in living cells observed by fluorescence correlation spectroscopy with one- and two-photon excitation, Biophys. J. 77 (1999) 2251–2265.

[6] R.H. Köhler, P. Schwille, W.W. Webb, M.R. Hanson, Active protein transport through plastid tubules: velocity quantified by fluorescence correlation spectroscopy, J. Cell Sci. 113 (2000) 3921–3930.

[7] N. Yoshida, M. Kinjo, M. Tamura, Microenvironment of endosomal aqueous phase investigated by the mobility of microparticles using fluorescence correlation spectroscopy, Biochem. Biophys. Res. Commun. 280 (2001) 312–318.

[8] K. Saito, E. Ito, Y. Takakuwa, M. Tamura, M. Kinjo, In situ observation of mobility and anchoring of PKC/βI in plasma membrane, FEBS Lett. 541 (2003) 126–131.

[9] U. Kettling, A. Koltermann, P. Schwille, M. Eigen, Real-time enzyme kinetics monitored by dual-color fluorescence cross-correlation spectroscopy, Proc. Natl. Acad. Sci. USA 95 (1998) 1416–1420.

[10] R. Rigler, Z. Földes-Papp, F.-J. Meyer-Almes, C. Sammet, M. Völcker, A. Schnetz, Fluorescence cross-correlation: a new concept for polymerase chain reaction, J. Biotechnol. 63 (1998) 97–109.

[11] T. Winkler, U. Kettling, A. Koltermann, M. Eigen, Confocal fluorescence coincidence analysis: an approach to ultra high-throughput screening, Proc. Natl. Acad. Sci. USA 96 (1999) 1375–1378.

[12] T. Kohl, K.G. Heinze, R. Kuhlemann, A. Koltermann, P. Schwille, A protease assay for two-photon cross-correlation and FRET analysis based solely on fluorescent proteins, Proc. Natl. Acad. Sci. USA 99 (2002) 12161–12166.

[13] K. Korn, P. Gardellin, B. Liao, M. Amacker, Å. Bergström, H. Björkman, A. Camacho, S. Dörhöfer, K. Dörre, J. Enström, T. Ericson, T. Favez, M. Gösch, A. Honegger, S. Jaccoud, M. Lapczyna, E. Litborn, P. Thyberg, H. Winter, R. Rigler, Gene expression analysis using single molecule detection, Nucleic Acids Res. 31 (2003) 89.

[14] Z. Földes-Papp, M. Kinjo, K. Saito, H. Kii, T. Takagi, M. Tamura, J.M. Costa, E. Birch-Hirschfeld, U. Demel, P. Thyberg, G.P. Tilz, C677T single nucleotide polymorphisms of the human methylene tetrahydrofolate reductase and specific identification, Mol. Diagn. 7 (2003) 99–111.

[15] T. Takagi, H. Kii, M. Kinjo, DNA measurements by using fluorescence correlation spectroscopy and two-color fluorescence cross-correlation spectroscopy, Curr. Pharm. Biotech. 5 (2004) 199–204.

[16] K. Bacia, I.V. Majoul, P. Schwille, Probing the endocytic pathway in live cells using dual-color fluorescence cross-correlation analysis, Biophys. J. 83 (2002) 1184–1193.

[17] S.A. Kim, K.G. Heinze, M.N. Waxham, P. Schwille, Intracellular calmodulin availability accessed with two-photon cross-correlation, Proc. Natl. Acad. Sci. USA 101 (2004) 105–110.

[18] R.E. Campbell, O. Tour, A.E. Palmer, P.A. Steinbach, G.S. Baird, D.A. Zacharias, R.Y. Tsien, A monomeric red fluorescent protein, Proc. Natl. Acad. Sci. USA 99 (2002) 7877–7882.

[19] S.I. Choi, H.W. Song, J.W. Moon, B.L. Seong, Recombinant enterokinase light chain with affinity tag: expression from Saccharomyces cerevisiae and its utilities in fusion protein technology, Biotechnol. Bioeng. 75 (2001) 718–724.

[20] Y. Shi, Mechanisms of caspase activation and inhibition during apoptosis, Mol. Cell 9 (2002) 459–470.

[21] K. Madin, T. Sawasaki, T. Ogasawara, Y. Endo, A highly efficient and robust cell-free protein synthesis system prepared from wheat embryos: plants apparently contain a suicide system directed at ribosomes, Proc. Natl. Acad. Sci. USA 97 (2000) 559–564.

[22] A. Miyawaki, A. Sawano, T. Kogure, Lighting up cells: labelling proteins with fluorophores, Nat. Cell Biol. 5 (2003) S1–S7.

ELSEVIER

Zinc sensing for cellular application

Kazuya Kikuchi[1,2,*], Kensuke Komatsu[1] and Tetsuo Nagano[1]

Numerous tools for Zn^{2+} sensing in living cells have become available in the past three years. Among them, fluorescence imaging using fluorescent sensor molecules has been the most popular approach. Some of these sensor molecules can be used to visualize Zn^{2+} in living cells. Some of the biological functions of Zn^{2+} have been clarified using these sensor molecules, especially in neuronal cells, which contain a high concentration of free Zn^{2+}.

Addresses
[1]Graduate School of Pharmaceutical Sciences, The University of Tokyo, 7-3-1 Hongo, Bunkyo-ku, Tokyo 113-0033, Japan
[2]PRESTO, JST, 4-1-8 Honcho Kawaguchi, Saitama, Japan
*e-mail: kkikuchi@mol.f.u-tokyo.ac.jp

Abbreviations

apoCA	apo-carbonic anhydrase
ESIPT	excited-state intramolecular proton transfer
FRET	fluorescence resonance energy transfer
GFP	green fluorescent protein
MF	mossy fiber
PEBBLE	Probe Encapsulated By Biologically Localized Embedding
TSQ	p-toluenesulfonamide quinoline

Introduction

Biological imaging of specific molecules can provide direct information of molecular functions in living systems. The most important breakthrough for this purpose is to create selective and sensitive sensing tools. Over the past three years, rapid improvements have been made in the development of Zn^{2+}-specific sensor molecules. Among several approaches, many fluorescent sensor molecules for the detection of chelatable Zn^{2+} have been reported. Some of these sensor molecules, such as Zinquin [1], ZnAF-2 [2**], FluoZin-3, FuraZin and RhodZin-3 [3**], have led to new findings about the role of Zn^{2+} in living systems. Fluorescent sensor molecules, which allow visualization of cations or enzyme activity in living cells by fluorescence microscopy, are useful tools for studying biological systems.

The adult human body contains up to several grams of Zn^{2+}, making this trace element the second most abun-

dant transition metal cation in biology [4]. Biological functions of Zn^{2+} have been reported for the protein-bound form. However, the biological function of free or loosely bound (labile, chelatable) Zn^{2+} is less certain. It is found at high concentrations, especially in the brain, pancreas and spermatozoa, and can be visualized by a fluorescent dye [5]. In the brain, labile Zn^{2+} is reported to exist at a concentration of several millimolar in the vesicles of presynaptic neurons, and is released by synaptic activity or depolarization, modulating the functions of certain ion channels and receptors [6]. Although the significance of Zn^{2+} in biological systems has been reported, its mechanisms of action are poorly understood.

Thus, fluorescent sensor molecules for detecting labile Zn^{2+} are needed to clarify the function of Zn^{2+}. Many fluorescent sensor molecules that can selectively detect Zn^{2+} have been reported in the past three years. A fluorescent sensor molecule typically consists of a fluorophore and an appropriate switch, which can induce characteristic fluorescence changes by Zn^{2+} binding, either in fluorescence intensity, in the excitation or emission wavelength, or both. Here, we describe recent progress in the development of these molecules, especially in the light of biological application. The chemical properties of sensor molecules that were reported after 2002 are summarized in Table 1.

Fluorescent sensors with short wavelength excitation

The first reported selective fluorescent sensor molecule for Zn^{2+} was p-toluenesulfonamide quinoline (TSQ) [7]. Several TSQ derivatives were synthesized to increase the water solubility. Among these derivatives, Zinquin can be used to monitor Zn^{2+} concentrations in living cells [1,5,8,9]. Zinquin forms a 1:2 complex by Zn^{2+} addition. Recently, detailed complex formation mechanisms have been reported by potentiometric studies on Zinquin [10].

Kimura and co-workers reported other derivatives of TSQ, whose fluorescence properties are improved by substitution of various functional groups onto the quinoline structure. 2-(9-Anthrylmethylamino)ethyl-apppended cyclen [11] and dansylamidoethylcyclen [12] were designed on the basis of the tight binding between carbonic anhydrase and arylsulfonamide, which is described later. Although the excitation wavelength of dansylamidoethylcyclen is in the undesirable ultraviolet range, its K_d value is relatively low, 5.5×10^{-13} M at pH 7.8, suggesting that this molecule would have high sensitivity. This sensor molecule is reported to be useful for the detection of apoptotic cells [12].
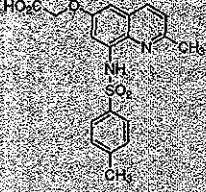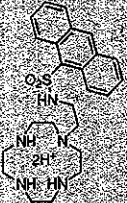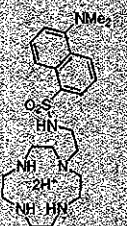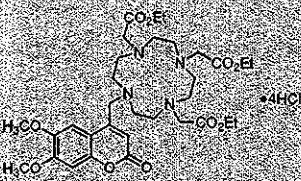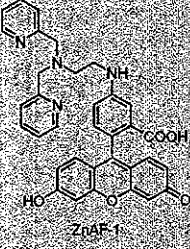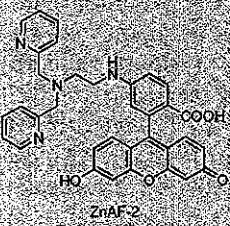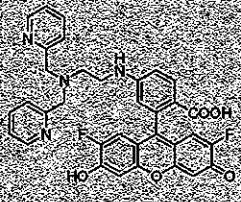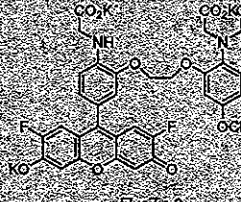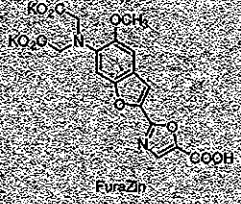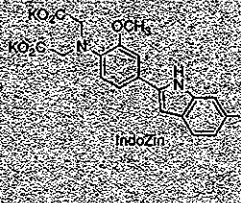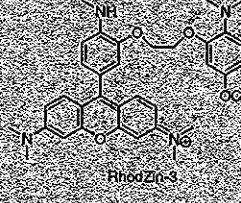
Table 1

Structure of fluorescent sensor molecules for Zn²⁺.

Structure of Sensor Molecule	K_d	Absorption maximum (nm) [without Zn²⁺]	Emission Maximum (nm) [without Zn²⁺]	Quantum Efficiency φ [without Zn²⁺]	Ref.	Biological application Ref.
	7 μM	370ᵃ	490		[1,5,8,9,10]	[1,8]
	0.02 nM	368ᵃ	416	[0.14] 0.44	[11]	
	0.55 nM	330ᵃ	[555] 528			[12]
	<1 μM	345ᵃ	448	>0.26	[13]	[13]
	0.78 nM	492ᵃ		[0.022] 0.21	[15,16]	
	2.7 nM	492ᵃ		[0.023] 0.32	[15,16]	[2••]

Table 1 Continued

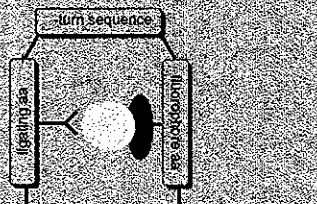| Structure of Sensor Molecule	K_d	Absorption maximum (nm) [without Zn^{2+}]	Emission Maximum (nm) [without Zn^{2+}]	Quantum Efficiency ϕ [without Zn^{2+}]	Ref	Biological application Ref
ZnAF-2F	5.5 nM	492[a]		[0.006] 0.24	[16]	
FluoZin-3	15.0 nM	488[a]	515[a]	[<0.005] [with TPEN] 0.43[a]	[18]	[18,19]
FuraZin	3.4 µM	[378] 330[b]	510		[20]	[37,38*]
IndoZin	3.0 µM	350[b]	[480] 395		[20]	
RhodZin-3	65 nM	545[a]			[21]	[3*]
Znpyr-4	0.65 nM	[506] 495[a]	[521] 515	[0.06] [with EDTA] 0.34	[24**]	
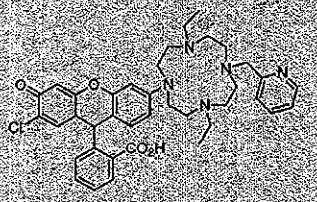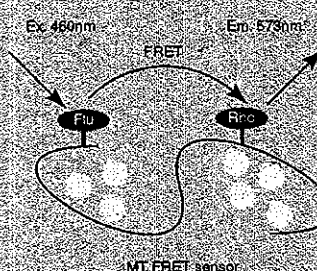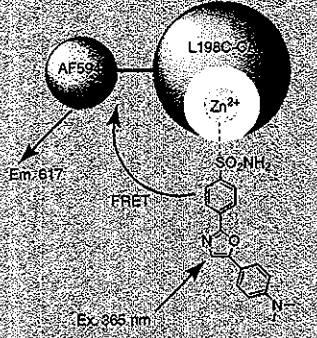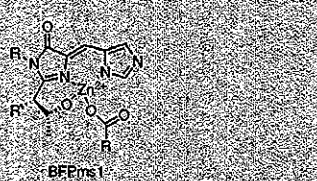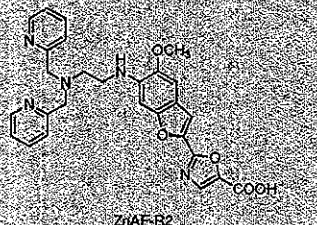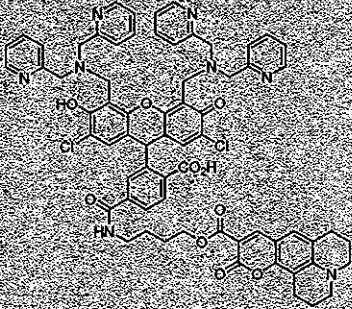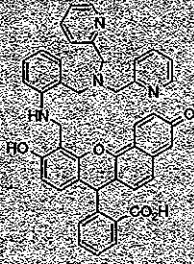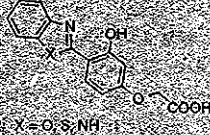
Table 1 Continued

Structure of Sensor Molecule	K_d	Absorption maximum (nm) [without Zn^{2+}]	Emission Maximum (nm) [without Zn^{2+}]	Quantum Efficiency ϕ [without Zn^{2+}]	Ref.	Biological application Ref.
Rhodafluor 2	13.5 µM	[514] 510ª	539	[0.36] [with EDTA] 0.56	[25]	
MT FRET sensor		460, 530ᵇ	519, 573		[26]	
	56 pM	385ᵇ	617		[27-29,30**]	
	Variant (10 nM ~ 12 µM)	360ª	[475] 500	[<0.005] 0.16	[34*]	
BFPms1					[35]	
ZnAF-R2	2.8 nM	[365] 335ᵇ	[495] 495	[0.17] 0.10	[36]	

Table 1 Continued

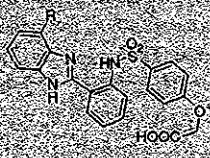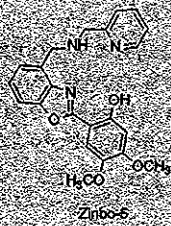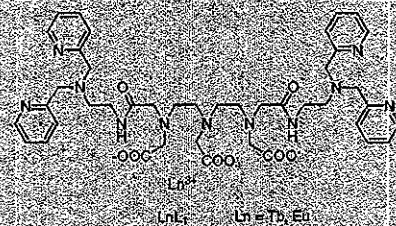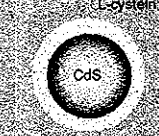| Structure of Sensor Molecule	K_d	Absorption maximum (nm) [without Zn^{2+}]	Emission Maximum (nm) [without Zn^{2+}]	Quantum Efficiency ϕ [without Zn^{2+}]	Ref.	Biological application Ref.
Coumazin-1		445, 505[b]	488, 534		[39]	
ZNP1	0.55 nM	503, 539[b]	528, 604	0.05	[40]	
X = O, S, NH	48 μM imidazole	[316] 332[b] imidazol	[355] 393 imidazol	[0.25] 0.23	[41*]	
1: R = H 2: R = (2-pyridyl)CH₂N(CH₃)CH₂[b] 3: R = (2-pyridyl CH₂)₂NCH₂[b]	(1) 31 μM (2) 0.59 nM (3) 0.79 pM	[329] 327[b] [329] 297[b] [332] 334[b]	[460] 406 [471] 415 [460] 406	[0.23] 0.22 [0.28] 0.17 [0.09] 0.21	[42,43]	
Zinbo-5	2.2 nM	356[b]	[407] 443	[0.02] 0.10	[44*]	

Structure of Sensor Molecule	K_d	Absorption maximum (nm) [without Zn^{2+}]	Emission Maximum (nm) [without Zn^{2+}]	Quantum Efficiency ϕ [without Zn^{2+}]	Ref.	Biological application Ref.
	2.6 nM	260	490, 546, 587		[45**]	
L-cysteine-capped CdS			[460]		[47]	

*One wavelength measurement; *Ratiometric measurement; *Long lifetime luminescence.

A coumarin-cyclen conjugate-based Zn^{2+} sensor molecule has been reported, whose fluorescence intensity was increased by Zn^{2+} addition. Although it takes ~30 min for imaging Zn^{2+} because the chelation is not quick, rat pituitary cells were stained without further derivatization; thus, the sensor molecule is membrane permeable [13].

Fluorescent sensor molecules based on fluorescein structure

Fluorescent sensor molecules that are excited by visible light are advantageous over sensors with shorter excitation, because excitation at ultraviolet wavelengths can cause cell damage, and cellular autofluorescence can interfere with the measurement. Fluorescein is one of the most widely used fluorophores in biological experiments and is advantageous in that it has a high quantum yield of fluorescence in aqueous solution, and its excitation wavelength is in the visible range. Thus, fluorescein can be a favorable fluorophore for Zn^{2+} fluorescent sensor molecules and several such sensors have been reported in the past couple of years that can be used in biological applications. The intensity of the fluorescence can be controlled by photo-induced electron transfer (PeT) between the xanthene ring, which acts as an electron acceptor and fluorophore, and the substituted benzoic acid moiety, which serves as electron donor [14]. As a receptor for Zn^{2+}, we chose TPEN (N,N,N',N'-tetrakis (2-pyridylmethyl)ethylenediamine) derivatives. We synthesized several compounds and ZnAFs were the best compounds, whose acceptor for Zn^{2+}, N,N-bis(2-pyridyl-methyl)ethylenediamine, is directly attached to the benzoic acid moiety via the aliphatic amine nitrogen. The dyes exhibited good properties as Zn^{2+} sensor molecules, and are specific for Zn^{2+} against other heavy metal ions and several cations, that exist at high concentration in

living cells such as Ca^{2+}, Mg^{2+}, Na^+ and K^+, which did not enhance the fluorescence intensity even at high concentration [15,16]. We applied ZnAF-2 to monitor extracellularly released Zn^{2+}, to clarify its function. Labile Zn^{2+} plays many physiologically important roles, especially in the central nervous system, where it is mainly stored in the synaptic vesicles of excitatory synapses, particularly the synaptic terminals of hippocampal mossy fibers (MFs), and is co-released with neurotransmitters in response to synaptic activity. When high-frequency stimulation was delivered to the MFs, the concentration of extracellular Zn^{2+} was immediately elevated in the stratum lucidum, and this was followed by a slight increase in the stratum radiatum adjacent to the stratum lucidum (SR proximal). Electrophysiological analyses revealed that NMDA-receptor-mediated synaptic responses (fEPSP$_{NMDA}$) in CA3 proximal stratum radiatum were inhibited in the immediate aftermath of MF activation and that this inhibition was no longer observed in the presence of a Zn^{2+}-chelating agent, which indicates that Zn^{2+} serves as a heterosynaptic mediator [2**]. From these results, Zn^{2+} can be the only messenger substance that is released presynaptically and moves into postsynaptic neurons after release of other neurotransmitters such as glutamate [17**].

Recently, Molecular Probes, Inc. (http://www.probes.com/) released a novel type of fluorescent sensor molecules, the FluoZin, FuraZin, IndoZin and RhodZin group. Among them, FuraZin and IndoZin were shown to be useful in ratiometric imaging of Zn^{2+} in living cells. Their chelator structure resembles the BAPTA (O,O'-bis(2-aminophenyl)ethylene-glycol-N,N,N',N'-tetraacetic acid) structure, which is used as a chelator in fluorescent sensor molecules for Ca^{2+}. FluoZin-3 has one acetic acid

removed from the BAPTA structure; its dissociation constant with Zn^{2+} is 15 nM, on addition of 100 μM Ca^{2+}, its fluorescence intensity is increased by about half of the increase upon Zn^{2+} addition [18]. FluoZin-3 was used to monitor Zn^{2+} release from pancreatic β-cells, with a high sensitivity of 10–40 nM and high temporal resolution of 16 ms/image [19]. FluoZin-3 showed much higher sensitivity against the previously reported ratiometric dyes Fura-Zin and Indo-Zin [20]. Fura-Zin was used to monitor Zn^{2+} release from neuronal cells [20]. RhodZin-3 was reported as a selective intra-mitochondrial Zn^{2+} sensor molecule [21]. RhodZin-3 showed large pH-independent fluorescence increase with high affinity for Zn^{2+} and no Ca^{2+} sensitivity at ≤ 40 μM. Sensi *et al.* applied Rhod-Zin-3 to cultured cortical neurons to monitor release of Zn^{2+} from mitochondria [3**]. It was shown that submicromolar Zn^{2+} can be found in mitochondria and membrane depolarization is induced by release of protein bound Zn^{2+}.

Lippard *et al.* reported the Zinpyr group, which contains dipicolylamine as the Zn^{2+} chelator [22,23]. Recently, they employed this design method for Zn^{2+} fluorescent sensor molecules by derivatizing the xanthene group with a Zn^{2+} chelator. They reported Zinpyr-4, which forms a 1:1 complex with Zn^{2+}, with a dissociation constant in the sub-nanomolar range at pH 7 (i.e. two orders of magnitude lower than that of dipicolylamine; 70 nM at pH 7), because of the additional coordination by the phenolic oxygen [24**]. The Zn^{2+} pool in rat brain hippocampal area can be visualized using Zinpyr-4. The hybrid chromophore with fluorescein and rhodamine was used for the fluorescent sensor Rhodafluor-2 [25].

Fluorescent sensor molecules based on peptide or proteins

In addition to the small-molecule fluorescent sensor, peptide- and protein-based fluorescent sensors have also been reported. Maret reported a metallothionein labeled with two fluorophores, fluorescein as a donor and rhodamine as an acceptor. This sensor peptide detects Zn^{2+} on the basis of the change in the efficiency of fluorescence resonance energy transfer (FRET) between two fluorophores. Upon binding of Zn^{2+} with the peptide, the conformational change brings the two fluorophores closer together, and enhances the efficiency of FRET, increasing the rhodamine fluorescence [26].

Thompson *et al.* have reported fluorescent sensing systems consisting of apo-carbonic anhydrase (apoCA) and fluorescent aryl sulfonamide (dansyl amide or the derivatives of 2-oxa-1,3-diazole-4-sulfonamide), which were originally used as inhibitors of carbonic anhydrase [27–29]. In the absence of Zn^{2+}, the fluorescent aryl sulfonamide cannot bind to apoCA. When Zn^{2+} is added, apoCA coordinates with Zn^{2+}, which allows binding of the fluorescent aryl sulfonamide to the holoenzyme. This

binding results in changes of fluorescence intensity, emission wavelength, lifetime and anisotropy, which make it possible to detect the change of Zn^{2+} concentration. This system has high sensitivity and selectivity, and can detect Zn^{2+} extracellularly released from hippocampal slices [30**].

Imperiali *et al.* designed peptide-based Zn^{2+} sensors with a modular scaffold [31–33]. In a recent paper, they employed amino acid derivatives of 8-hyrodoxy-quinoline as Zn^{2+}-sensitive fluorescent chelators positioned opposite the site of an additionally chelating peptide. These two peptides, Zn^{2+} chelator and fluorescent sensor sequence, were bridged with a β-turn peptide for appropriate positioning of the two moieties. The peptide sequence was optimized and the highest affinity was 9.6 nM. The affinity can be tuned from 10 nM to 12 μM by the selection of the peptide sequence around the fluorescent amino acid [34*].

Protein-based sensor molecules, which can detect Zn^{2+}, based on mutated green fluorescent proteins (GFPs) are also reported. These sensor molecules would be useful because they can be introduced non-invasively into the cells by transfection, and be targeted to specific tissues, organelles or cellular localizations. Getzoff *et al.* reported a GFP mutant designed to bind Zn^{2+} at its conjugated chromophore site, resulting in enhancement of its fluorescence intensity [35]. Mutated GFP-based sensors are potentially advantageous, and the sensor molecules reported to date can be improved in terms of sensitivity and complexation rate.

Fluorescent sensor molecules for ratiometric measurement

Recently, other types of fluorescent probes have also been reported. One particularly interesting type is probes that enable ratiometric imaging. This is a technique that involves observing the changes in the ratio of fluorescence intensities at two wavelengths. Compared with the measurement of the fluorescence intensity at only one wavelength, this method reduces artefacts by minimizing the influence of extraneous factors, such as the changes of the probe concentration and excitation light intensity. Based on the structure of Fura-2, novel fluorescent probes have been developed for ratiometric measurement of Zn^{2+}: FuraZin, whose chelator structure is that of FluoZin-1; and ZnAF-R2, whose chelator structure is that of ZnAF-2 [36]. Their selectivity for Zn^{2+} over other cations and their dissociation constants are similar to fluorescent sensor molecules with the same type of chelators. Reynolds *et al.* reported the significance of intracellular sensor concentration for monitoring Zn^{2+} concentration by the comparison of ratiometric measurement using FuraZin (K_d ~3 μM) and Magfura-2 (K_d ~0.02 μM) [37]. Eide *et al.* used FuraZin to monitor Zn^{2+} level in the yeast *Saccharomyces cerevisiae* for

clarifying the function of *ZRC1*, which works in storage and detoxification of excess Zn^{2+} [38°]. It was shown that Zrc1 is required for restoration of Zn^{2+} into the vacuole during Zn^{2+} shock. The conjugated sensor Coumazin-1, which combines a coumarin fluorophore with Zynpyr-1, was reported by Lippard *et al.* to monitor membrane-penetrated fluorescent sensor concentration simultaneously with Zn^{2+} concentration for ratiometric measurement [39]. They also reported Zin-naphthopyr 1 (ZNP1), which was developed by extending the xanthene moiety by naphthalene. Its spectral change is based on tautomeric deprotonation of Zinpyr derivative, resulting in emission intensity augmentation at two wavelengths by Zn^{2+} addition [40].

An interesting concept for ratiometric measurements was reported by Fahrni *et al.* and is based on Zn^{2+}-induced inhibition of excited-state intramolecular proton transfer (ESIPT) [41°°,42]. In these sensors, the intramolecular hydrogen bond that is responsible for the ESIPT process is replaced by Zn^{2+} coordination, resulting in a significant shift of the emission wavelength. They further derivatized these lead compounds to provide ratiometric Zn^{2+} sensors with various affinities for Zn^{2+} [43]. A similar approach was reported by O'Halloran *et al.* to design Zinbo-5 for ratiometric measurements by two-photon excitation microscopy [44°].

Other types of fluorescent sensor molecules
Another new type is a long-lifetime luminescent sensor molecule with lanthanide-complex structures. Luminescent lanthanide complexes, in particular Tb^{3+} and Eu^{3+} complexes, have long luminescence lifetimes of the order of milliseconds. Zn^{2+} sensor molecules were reported, based on the conjugation of diethylenetriaminepentaacetic acid (DTPA)-bisamide lanthanide complex with two picolylamide Zn^{2+} chelators [45°°]. For Tb^{3+} complexes, the emission intensity was increased by the addition of Zn^{2+}, and their lifetimes were in the millisecond range. This increase is ascribed to the efficiency of intramolecular energy transfer from the pyridyl group to the lanthanide ion, which is induced by the proximity effect from Zn^{2+} chelation.

Kopelman *et al.* reported a nanosensor for Zn^{2+} based on PEBBLE (Probe Encapsulated By Biologically Localized Embedding) [46]. The PEBBLE for Zn^{2+} is a polymer matrix conjugated with two entrapped fluorophores, a Zn^{2+}-sensitive fluorophore and a reference fluorophore. The sensor was selective for Zn^{2+} in the concentration range of 4–50 μM of Zn^{2+}. The advantage of this sensor is its photostability and insensitivity to interference from proteins.

Rozenzweig *et al.* reported a conjugate of water-soluble luminescent CdS quantum dots with L-cysteine capping for Zn^{2+} chelation [47]. The conjugated quantum dots

can detect Zn^{2+} in the submicromolar range by enhancing the luminescence. This luminescence enhancement by Zn^{2+} addition can be attributed to activation of surface states. This is the first report to show the utilization of quantum dots as selective ion sensors in the aqueous phase.

Conclusion
Reported Zn^{2+} fluorescent sensors can be used for monitoring intracellular Zn^{2+} concentration changes. However, all the reported fluorescent sensor molecules are not necessarily appropriate in all the studies for clarifying the physiological function of Zn^{2+}. So, careful consideration in both the chemical and biological properties of the sensor molecules is necessary. The effective concentration range and the kinetic parameters, such as association and dissociation rates constant, are important. In addition to these chemical parameters, biological parameters, for example, cell-membrane permeability, intracellular localization, and the toxicity of the excitation light and the sensor molecules themselves to the cells, should also be considered. The purpose of the measurement is also important. For example, to study the distribution of Zn^{2+} in biological samples with high resolution and no requirement for temporal resolution, a staining method, such as Timm's staining, measured by electron microscopy would be the most suitable [48,49]. Possible future directions for the development of Zn^{2+} sensor molecules include covering of a wider K_d range, shifting the excitation wavelength towards the infrared region, targeting the probe to specific subcellular locations, and improving the dynamic range of ratiometric sensors. These goals will provide a variety of new sensor molecules that will stimulate new research and further the understanding of the role of Zn^{2+} in biology.

Acknowledgements

References and recommended reading
Papers of particular interest, published within the annual period of review, have beenhighlighted as:

• of special interest
•• of outstanding interest

1. Zalewski PD, Forbes IJ, Betts WH: **Correlation of apoptosis with change in intracellular labile Zn(II) using Zinquin (2-methyl-8-*p*-toluenesulphonamido-6-quinolyloxy)acetic acid, a new specific fluorescent-probe for Zn(II).** *Biochem J* 1993, **296**:403-408.

2. Ueno S, Tsukamoto M, Hirano T, Kikuchi K, Yamada MK,
•• Nishiyama M, Nagano T, Matsuki N, Ikegaya Y: **Mossy fiber Zn^{2+} spillover modulates heterosynaptic N-methyl-D-aspartate receptor activity in hippocampal CA3 circuits.** *J Cell Biol* 2002, **158**:215-220.
The authors describe how Zn^{2+} is released from mossy fibre to play a role as an inhibitor of glutamate receptor function.

3. Sensi SL, Ton-That D, Sullivan PG, Jonas EA, Gee KR,
•• Kaczmarek LK, Weiss JH: **Modulation of mitochondrial function**

by endogenous Zn^{2+} pools. *Proc Natl Acad Sci USA* 2003, 100:6157-6162.
The cationic Zn^{2+} sensor molecule RhodZin-3 accumulates in mitochondria and reports Zn^{2+} release by depolarization.

4. da Silva JJRF, Williams RJP: **Zinc: Lewis acid catalysis and regulation.** In *The Biological Chemistry of Elements: The Inorganic Chemistry of Life, 2nd ed.* New York: Oxford UP; 2001:315-339.

5. Zalewski PD, Jian X, Soon LLL, Breed WG, Seamark RF, Lincoln SF, Ward AD, Sun FZ: **Changes in distribution of labile zinc in mouse spermatozoa during maturation in the epididymis assessed by the fluorophore Zinquin.** *Reprod Fertil Dev* 1996, 8:1097-1105.

6. Weiss JH, Sensi SL, Koh JY: **Zn^{2+}: a novel ionic mediator of neural injury in brain disease.** *Trends Pharm Sci* 2000, 21:395-401.

7. Frederickson CJ, Kasarskis EJ, Ringo D, Frederickson RE: **A quinoline fluorescence method for visualizing and assaying the histochemically reactive zinc (bouton zinc) in the brain.** *J Neurosci Methods* 1987, 20:91-103.

8. Zalewski PD, Forbes IJ, Seamark RF, Borlinghaus R, Betts WH, Lincoln SF, Ward AD: **Flux of intracellular labile zinc during apoptosis (gene-directed cell death) revealed by specific chemical probe, Zinquin.** *Chem Biol* 1994, 1:153-161.

9. Kimber MC, Mahadevan IB, Lincoln SF, Ward AD, Tiekink ERT: **The synthesis and fluorescent properties of analogues of the zinc(II) specific fluorophore Zinquin ester.** *J Org Chem* 2000, 65:8204-8209.

10. Hendrickson KM, Geue JP, Wyness O, Lincoln SF, Ward AD: **Coordination and fluorescence of the intracellular Zn^{2+} probe 2-methyl-8-(4-toluenesulfonamido)-6-quinolyloxy acetic acid (Zinquin a) in ternary Zn^{2+} complexes.** *J Am Chem Soc* 2003, 125:3889-3895.

11. Aoki S, Kaido S, Fujioka H, Kimura E: **A new zinc(II) fluorophore 2-(9-anthrylmethylamino)ethyl- appended 1,4,7,10-tetraazacyclododecane.** *Inorg Chem* 2003, 42:1023-1030.

12. Kimura E, Aoki S, Kikuta E, Koike T: **A macrocyclic zinc(II) fluorophore as a detector of apoptosis.** *Proc Natl Acad Sci USA* 2003, 100:3731-3736.

13. Lim NC, Yao L, Freake HC, Bruckner C: **Synthesis of a fluorescent chemosensor suitable for the imaging of Zinc(II) in live cells.** *Bioorg Med Chem Lett* 2003, 13:2251-2254.

14. Hirano T, Kikuchi K, Urano Y, Higuchi T, Nagano T: **Novel zinc fluorescent probes excitable with visible light for biological applications.** *Angew Chem Int Ed Engl* 2000, 39:1052-1054.

15. Hirano T, Kikuchi K, Urano Y, Higuchi T, Nagano T: **Highly zinc-selective fluorescent sensor molecules suitable for biological applications.** *J Am Chem Soc* 2000, 122:12399-12400.

16. Hirano T, Kikuchi K, Urano Y, Nagano T: **Improvement and biological applications of fluorescent probes for zinc, ZnAFs.** *J Am Chem Soc* 2002, 124:6555-6562.

17. Lee YV, Hough CJ, Sarvey JM: **Do we need zinc to think?**
•• *Sci STKE* 2003, pe19.
The authors summarize recent reports on Zn^{2+} function in neuronal systems.

18. Gee KR, Zhou ZL, Qian WJ, Kennedy R: **Detection and imaging of zinc secretion from pancreatic beta- cells using a new fluorescent zinc indicator.** *J Am Chem Soc* 2002, 124:776-778.

19. Qian WJ, Gee KR, Kennedy RT: **Imaging of Zn^{2+} release from pancreatic beta-cells at the level of single exocytotic events.** *Anal Chem* 2003, 75:3468-3475.

20. Gee KR, Zhou ZL, Ton-That D, Sensi SL, Weiss JH: **Measuring zinc in living cells. A new generation of sensitive and selective fluorescent probes.** *Cell Calcium* 2002, 31:245-251.

21. Sensi SL, Ton-That D, Weiss JH, Rothe A, Gee KR: **A new mitochondrial fluorescent zinc sensor.** *Cell Calcium* 2003, 34:281-284.

22. Walkup GK, Burdette SC, Lippard SJ, Tsien RY: **A new cell-permeable fluorescent probe for Zn^{2+}.** *J Am Chem Soc* 2000, 122:5644-5645.

23. Burdette SC, Walkup GK, Springler B, Tsien RY, Lippard SJ: **Fluorescent sensors for Zn^{2+} based on fluorescein platform: synthesis, properties and intracellular distribution.** *J Am Chem Soc* 2001, 123:7831-7841.

24. Burdette SC, Frederickson CJ, Bu WM, Lippard SJ: **ZP4, an**
•• **improved neuronal Zn^{2+} sensor of the Zinpyr family.** *J Am Chem Soc* 2003, 125:1778-1787.
The recent advances in Zinpyr family is reported, which include 1:1 complex formation and high quantum yield.

25. Burdette SC, Lippard SJ: **The rhodafluor family. An initial study of potential ratiometric fluorescent sensors for Zn^{2+}.** *Inorg Chem* 2002, 41:6816-6823.

26. Hong SH, Maret W: **A fluorescence resonance energy transfer sensor for the β-domain of metallothionein.** *Proc Natl Acad Sci USA* 2003, 100:2255-2260.

27. Thompson RB, Jones ER: **Enzyme-based fiber optic zinc biosensor.** *Anal Chem* 1993, 65:730-734.

28. Thompson RB, Patchan MW: **Lifetime-based fluorescence energy-transfer biosensing of zinc.** *Anal Biochem* 1995, 227:123-128.

29. Thompson RB, Maliwal BP, Fierke CA: **Expanded dynamic range of free zinc ion determination by fluorescence anisotropy.** *Anal Chem* 1998, 70:1749-1754.

30. Thompson RB, Cramer ML, Bozym R, Fierke CA: **Excitation**
•• **ratiometric fluorescent biosensor for zinc ion at picomolar levels.** *J Biomed Opt* 2002, 7:555-560.
The authors report practical sensing system of Zn^{2+} using protein scaffold of Zn^{2+} binding protein.

31. Walkup GK, Imperiali B: **Design and evaluation of a peptidyl fluorescent chemosensor for divalent zinc.** *J Am Chem Soc* 1996, 118:3053-3054.

32. Walkup GK, Imperiali B: **Fluorescent chemosensors for divalent zinc based on zinc finger domains. Enhanced oxidative stability, metal binding affinity, and structural and functional characterization.** *J Am Chem Soc* 1997, 119:3443-3450.

33. Walkup GK, Imperiali B: **Stereoselective synthesis of fluorescent α-amino acids containing oxine (8-hydroxyquinoline) and their peptide incorporation in chemosensors for divalent zinc.** *J Org Chem* 1998, 63:6727-6731.

34. Shults MD, Pearce DA, Imperiali B: **Modular and tunable**
• **chemosensor scaffold for divalent zinc.** *J Am Chem Soc* 2003, 125:10591-10597.
The authors used a designed peptide scaffold with fluorophore and Zn^{2+} chelator, which enhances the specificity and selectivity for Zn^{2+} sensing.

35. Barondeau DP, Kassmann CJ, Tainer JA, Getzoff ED: **Structural chemistry of a green fluorescent protein Zn biosensor.** *J Am Chem Soc* 2002, 124:3522-3524.

36. Maruyama S, Kikuchi K, Hirano T, Urano Y, Nagano T: **A novel, cell-permeable, fluorescent probe for ratiometric imaging of zinc ion.** *J Am Chem Soc* 2002, 124:10650-10651.

37. Dineley KE, Malaiyandi LM, Reynolds IJ: **A reevaluation of neuronal zinc measurements: Artifacts associated with high intracellular dye concentration.** *Mol Pharmacol* 2002, 62:618-627.

38. MacDiarmid CW, Milanick MA, Eide DJ: **Induction of the ZRC1**
• **metal tolerance gene in zinc-limited yeast confers resistance to zinc shock.** *J Biol Chem* 2003, 278:15065-15072.
It is shown elegantly by the authors that detoxification of Zn^{2+} in yeast is regulated by the transcription of Zn^{2+}-sensitive proteins.

39. Woodroofe CC, Lippard SJ: **A novel two-fluorophore approach to ratiometric sensing of Zn^{2+}.** *J Am Chem Soc* 2003, 125:11458-11459.

40. Chang CJ, Jaworski J, Nolan EM, Sheng M, Lippard SJ: **A tautomeric zinc sensor for ratiometric fluorescence imaging: application of nitric oxide-induced release of intracellular zinc.** *Proc Natl Acad Sci USA* 2004, 101:1129-1134.

41. Henary MM, Fahrni CJ: **Excited state intramolecular proton**
•• **transfer and metal ion complexation of 2-(2'-hydroxyphenyl)benzazoles in aqueous solution.** *J Phys Chem A* 2002, 106:5210-5220.

The authors describe a physico-chemical basis of excited-state intramolecular proton transfer for designing ratiometric metallo-sensitive sensor molecules.

42. Fahrni CJ, Henary MM, VanDerveer DG: **Excited state intramolecular proton transfer in 2-(2′-tosylaminophenyl)benzimidazole.** *J Phys Chem A* 2002, 106:7655-7663.

43. Henary MM, Wu Y, Fahrni CJ: **Zinc(II)-selective ratiometric fluorescent sensors based on inhibition of excited-state intramolecular proton transfer.** *Chem Eur J* 2004, in press.

44. Taki M, Wolford JL, O'Halloran TV: **Emission ratiometric imaging**
•   **of intracellular zinc: design of a benzoxazole fluorescent sensor and its application in two-photon microscopy.** *J Am Chem Soc* 2004, 126:712-713.
The authors report a benzoxazole derivative for emission ratiometric measurement by Zn^{2+} addition.

45. Hanaoka K, Kikuchi K, Kojima H, Urano Y, Nagano T: **Selective**
•• **detection of zinc ions with novel luminescent lanthanide probes.** *Angew Chem Int Edit* 2003, 42:2996-2999.

A Tb^{3+} complex with additional chelating ligands for Zn^{2+} was synthesized, and long life-time luminescence was augmented by Zn^{2+} addition.

46. Sumner JP, Aylott JW, Monson E, Kopelman R: **A fluorescent PEBBLE nanosensor for intracellular free zinc.** *Analyst* 2002, 127:11-16.

47. Chen Y, Rosenzweig Z: **Luminescent CdS quantum dots as selective ion probes.** *Anal Chem* 2002, 74:5132-5138.

48. Timm F: **Zur Histochemie der Schwermetalle. Das Sulfid-Silberverfahren.** *Dtsch Z Gesamte Gerichtl Med* 1958, 46:706-711. [Title translation: Histochemistry of heavy metals; the sulfide-silver procedure].

49. Danscher G, Juhl S, Stoltenberg M, Krunderup B, Schrøder HD, Andreasen A: **Autometallographic silver enhancement of zinc sulfide crystals created in cryostat sections from human brain biopsies: a new technique that makes it feasible to demonstrate zinc ions in tissue sections from biopsies and early autopsy material.** *J Histochem Cytochem* 1997, 45:1503-1510.

Molecular basis of the high-affinity activation of type 1 ryanodine receptors by imperatoxin A

Chul Won LEE*, Eun Hui LEE*, Koh TAKEUCHI†, Hideo TAKAHASHI†, Ichio SHIMADA†, Kazuki SATO‡, Song Yub SHIN§, Do Han KIM* and Jae Il KIM*[1]

*Department of Life Science, Kwangju Institute of Science and Technology, Kwangju 500-712, South Korea, †Graduate School of Pharmaceutical Sciences, The University of Tokyo, Tokyo 113-0033, Japan, ‡Department of Environmental Science, Fukuoka Women's University, Fukuoka 813-8529, Japan, and §Research Center for Proteineous Materials, Chosun University, Kwangju 501-759, South Korea

Both imperatoxin A (IpTx$_a$), a 33-residue peptide toxin from scorpion venom, and peptide A, derived from the II–III loop of dihydropyridine receptor (DHPR), interact specifically with the skeletal ryanodine receptor (RyR1), which is a Ca^{2+}-release channel in the sarcoplasmic reticulum, but with considerably different affinities. IpTx$_a$ activates RyR1 with nanomolar affinity, whereas peptide A activates RyR1 at micromolar concentrations. To investigate the molecular basis for high-affinity activation of RyR1 by IpTx$_a$, we have determined the NMR solution structure of IpTx$_a$, and identified its functional surface by using alanine-scanning analogues. A detailed comparison of the functional surface profiles for two peptide activators revealed that IpTx$_a$ exhibits a large functional surface area (approx. 1900 Å^2, where 1 Å = 0.1 nm), based on a short double-stranded antiparallel β-sheet structure, while peptide A bears a much smaller functional surface area (approx. 800 Å^2), with the five consecutive basic residues (Arg^{681}, Lys^{682}, Arg^{683}, Arg^{684} and Lys^{685}) being clustered at the C-terminal end of the α-helix. The functional surface of IpTx$_a$ is composed of six essential residues (Leu^7, Lys^{22}, Arg^{23}, Arg^{24}, Arg^{31} and Arg^{33}) and several other important residues (His^6, Lys^8, Arg^9, Lys^{11}, Lys^{19}, Lys^{20}, Gly^{25}, Thr^{26}, Asn^{27} and Lys^{30}), indicating that amino acid residues involved in RyR1 activation make up over the half of the toxin molecule with the exception of cysteine residues. Taken together, these results suggest that the site where peptide A binds to RyR1 belongs to a subset of macrosites capable of being occupied by IpTx$_a$, resulting in differing the affinity and the mode of activation.

Key words: excitation–contraction coupling, imperatoxin A, NMR, peptide A, ryanodine receptor, solution structure.

INTRODUCTION

In cardiac and skeletal muscle, the ryanodine receptor (RyR) is a Ca^{2+}-release channel in the sarcoplasmic reticulum (SR) and the dihydropyridine receptor (DHPR) is a voltage-gated L-type Ca^{2+} channel. These two receptors play central roles in the sarcolemma excitation–contraction (E–C) coupling that links an electrical stimulus (depolarization) to release of Ca^{2+} from the SR [1]. Cardiac and skeletal muscles express different subtypes of DHPRs and RyRs, causing tissue-specific E–C coupling. In cardiac muscle, E–C coupling is induced by the entry of extracellular Ca^{2+} through DHPR, whereas skeletal type E–C coupling requires a direct physical coupling between DHPR and RyR [2,3]. Evidence supporting this physical coupling between skeletal DHPR and RyR1 (skeletal type RyR) includes successful co-immunoprecipitation [4] and identification of regions involved in the physical coupling between the two channels. Specifically, interactions have been observed between portions of the α_1 subunit of DHPR, including the II–III loop, the III–IV loop and the C-terminal segment, and the Arg^{1076}–Asp^{1112} region of RyR1 [5–12]. It has been proposed that these interactions cause orthograde signalling from DHPR to RyR1 for activation of RyR1, and retrograde signalling from RyR1 to DHPR for RyR1-mediated enhancement of Ca^{2+} current [11,13].

Imperatoxin A (IpTx$_a$), a 33-amino-acid peptide from the venom of the scorpion, *Pandinus imperator*, was the first peptide toxin found to activate RyR1 with high potency and affinity, and it has been used in several biochemical and biophysical studies related to the E–C coupling [14,15]. Interestingly, it has been suggested that IpTx$_a$ activates RyR1 by mimicking a domain of DHPR that is critical for triggering Ca^{2+} release. Using synthetic peptides corresponding to small segments of the II–III loop in skeletal DHPR, El-Hayek et al. [7] found that only the N-terminal portion (peptide A; Thr^{671}–Leu^{690}) was capable of activating RyR1, and subsequently identified a ten-residue active region (Arg^{681}–Leu^{690}) [16]. In addition, Gurrola et al. [17] reported that a peptide A-containing segment (Glu^{666}–Leu^{690}) might bind to the same RyR1 site as IpTx$_a$, as shown by the results of competitive binding of ^{125}I-labelled IpTx$_a$ to the SR. This was additionally supported by the report that both peptides produced almost identical changes, with non-additive effects, in RyR1 gating characteristics [18]. Although these observations strongly suggested that IpTx$_a$ and peptide A share a common binding site on RyR1, the two peptide activators show very low sequence identity (approx. 18 %), very different molecular structures, and considerably different affinities in RyR1 activation. IpTx$_a$ activates RyR1 with nanomolar affinity, whereas peptide A activates RyR1 at micromolar concentrations [17].

In order to examine the molecular basis by which two peptide activators, IpTx$_a$ and peptide A, act at a common site on RyR1 with different affinities, the present study reports the solution structure of IpTx$_a$ as determined by NMR spectroscopy and

dynamic simulated annealing calculations, and we have combined this structural information with the results of [3H]ryanodine binding assays using alanine-scanning analogues. On the basis of the structure–activity relationships for IpTx$_a$, we propose that the peptide A-binding site on RyR1 belongs to a subset of macrosites capable of being occupied by IpTx$_a$, resulting in the observed differences in RyR1 affinity and activation. Furthermore, a comparative structural analysis with the cone-snail ω-conotoxin MVIIC (ω-CTX-MVIIC), a neuronal P/Q-type calcium-channel blocker, revealed that the characteristic shape of charged surface rather than globular shape is important to the interaction with RyR1, thus providing a structural insight for the specific interaction mode of RyR1-targeting peptide effectors.

MATERIALS AND METHODS

Materials

Fmoc (9-fluorenylmethoxycarbonyl) amino acids and other reagents used for peptide synthesis were obtained from Applied Biosystems. Fmoc-preloaded resin was obtained from Watanabe Chemical Industries (Hiroshima, Japan). [3H]ryanodine was obtained from NEN Life Science Products (Torrance, CA, U.S.A.). All other regents were of high-purity reagent grade from Sigma Chemical Co.

Peptide synthesis of wild-type IpTx$_a$ (wIpTx$_a$) and analogues

Peptide synthesis was conducted on an Applied Biosystems model 433A peptide synthesizer. The linear precursors of wIpTx$_a$ and alanine-scanning analogues were synthesized by solid-phase Fmoc chemistry starting from Fmoc-Arg(2,2,5,7,8-pentamethyl-chroman-6-sulphonyl)-Alko or Fmoc-Ala-Alko resin and using a variety of blocking groups for amino acid protection. After cleavage by trifluoroacetic acid, crude linear peptides were extracted with 2 M ethanoic acid, diluted to final peptide concentrations of 25 μM in a solution of 1 M ammonium acetate and 2.5 mM reduced/0.25 mM oxidized glutathione adjusted to pH 7.8 with aqueous NH$_4$OH, and stirred slowly at 4 °C for 2–3 days. The folding reactions were monitored by HPLC. The crude oxidized products were purified by successive chromatography with CM-cellulose CM-52 and preparative HPLC with C$_{18}$ silica columns. The purity of all analogues was confirmed by analytical HPLC and MALDI–TOF-MS (matrix-assisted laser-desorption ionization–time-of-flight MS) measurements.

CD measurements of wIpTx$_a$ and analogues

CD spectra were measured on a JASCO J-750 spectropolarimeter in solution (0.01 M sodium phosphate in water, pH 7.0) at 20 °C with a quartz cell of path length 1 mm. The spectra were expressed as molecular ellipticity [θ] in deg · cm^2 · dmol^{-1}.

NMR measurements of wIpTx$_a$

NMR spectra were recorded on a Bruker DRX 600 spectrometer. All two-dimensional NMR experiments {i.e. DQF-COSY (double-quantum-filtered COSY) [19], E-COSY (exclusive COSY) [20], HOHAHA (homonuclear Hartmann–Hahn) [21] and NOESY [22]} were performed with standard pulse sequences and phase cycling. HOHAHA spectra were recorded with mixing times of 60 and 80 ms. NOESY spectra were recorded with mixing times of 100, 200 and 300 ms. In all experiments, 512 increments of 2048 data points were recorded with 64–128 trans-

ients and were zero-filled once along the t_1 dimension. A complete set of the two-dimensional spectra was recorded at 27 °C (pH 3.4). Synthesized wIpTx$_a$ (a final concentration of 5 mM) was dissolved in 0.2 ml of water containing ^{2}H$_2$O at 10 % (v/v) or 99.9 % (v/v). Spectra were processed and analysed with Bruker XWIN-NMR software.

Structure calculations of wIpTx$_a$

Observed NOE (nuclear Overhauser effect) data were classified into four distance ranges, 1.8–2.7, 1.8–3.5, 1.8–5.0 and 1.8–6.0 Å (1 Å = 0.1 nm), corresponding to strong, medium, weak and very weak NOE values respectively. Pseudo-atoms were used for the methyl protons or the non-stereospecifically assigned methylene protons [23]. Correcting factors for the use of pseudo-atoms were added to the distance constraints. In addition, 0.5 Å was added to the distance constraints involving methyl protons [24]. For each disulphide bond, three distance constraints, $S(i)$-$S(j)$, $S(i)$-$C^\beta(j)$ and $S(j)$-$C^\beta(i)$, were used with target values set to 2.02($\pm$ 0.02), 2.99($\pm$ 0.5) and 2.99($\pm$ 0.5) Å respectively [25].

All calculations were performed using the X-PLOR 3.1 program [26] running on a SGI O2 workstation. Three-dimensional structures were calculated on the basis of distance and torsion angle constraints experimentally derived with dynamic simulated annealing protocols. The 20 best structures were chosen for structural analysis, based on the X-PLOR energy and best fit. The structures were analysed with the PROCHECK-NMR [27] and PROMITIF [28] software packages. Structural figures were generated with the MOLMOL program [29] and the INSIGHT II 2000 program (Accelrys Inc.).

Isolation of SR vesicles

A heavy fraction of SR was prepared from rabbit back and leg fast twitch muscles with a modification of the previously described method [30]. Briefly, about 150 g of muscle was homogenized in a Waring blender with 4 vol. of 2.5 mM NaOH for six bursts of 20 s at intervals of 3 min. During the homogenization, the pH was adjusted to 6.8 with NaOH. The suspension was centrifuged at 10 000 g for 3 min in a No. 9 rotor in a Hanil Supra22K centrifuge. The supernatant was filtered through eight layers of cheesecloth and then through Whatman filter paper (No. 4). After re-adjusting the pH to 6.8, if necessary, the filtrate was centrifuged again at 17 000 g for 30 min in the above apparatus. The pellets were suspended in the final buffer consisting of 0.15 M KCl, 20 mM Mops (pH 6.8) and 0.3 M sucrose in the presence of the following protease inhibitors: pepstatin (1 μM), leupeptin (1 μM), PMSF (100 μM) and trypsin inhibitor (1 μM). The suspension was centrifuged again at 17 000 g for 30 min in a No. 7 rotor in a Hanil Supra22K centrifuge. The pellets were resuspended in the same final buffer and the final protein concentration was determined by the Bradford method [30a] using BSA as the standard. The obtained SR was quickly frozen in liquid N$_2$ and then stored at − 70 °C until use.

[3H]Ryanodine binding assay with wIpTx$_a$ and analogues

[3H]Ryanodine binding to rabbit skeletal SR vesicles was performed as previously described [31] with some modifications. Briefly, 0.04 mg of skeletal SR vesicles was incubated with various concentrations of wIpTx$_a$, or one of the analogues, for 2 h at 37 °C in a reaction mixture of 250 μl {0.2 M KCl, 20 mM Mops (pH 7.3), 5 nM [3H]ryanodine and 10 μM free Ca^{2+}}. After incubation, 100 μl of poly(ethylene glycol) (PEG) solution (30 %